Reconfigurable Acoustic Arrays With Deployable Structure Based on a Hoberman–Miura System Synthesis

Ningxiner Zhao
Department of Mechanical and Aerospace Engineering,
The Ohio State University,
Columbus, OH 43210
e-mail: zhao.2684@osu.edu

Ryan L. Harne[1]
Department of Mechanical and Aerospace Engineering,
The Ohio State University,
Columbus, OH 16802
e-mail: harne.3@osu.edu

Curved surfaces are often used to radiate and focus acoustic waves. Yet, when tessellated into reconfigurable surfaces for sake of deployability needs, origami-inspired acoustic arrays may be challenging to hold into curved shape and may not retain flat foldability. On the other hand, deployable mechanisms such as the Hoberman ring are as low-dimensional as many origami tessellations and may maintain curved shape with ease due to ideal rigid bar compositions. This research explores an interface between a Hoberman ring and Miura-ori tessellation that maintain kinematic and geometric compatibility for sake of maintaining curved shapes for sound focusing. The Miura-ori facets are considered to vibrate like baffled pistons and generate acoustic waves that radiate from the ring structure. An analytical model is built to reveal the near field acoustic behavior of acoustic arrays resulting from a Hoberman–Miura system synthesis. Acoustic wave focusing capability is scrutinized and validated through proof-of-principle experiments. Studies reveal wave focusing phenomena distinct to this manifestation of the acoustic array and uncover design and operational influences on wave focusing effectiveness. The results encourage exploration of new interfaces between reconfigurable mechanisms and origami devices where low-dimensional shape change is desired. [DOI: 10.1115/1.4048745]

Keywords: origami mechanisms, acoustic waves, reconfigurable structure

1 Introduction

Acoustic wave focusing has broad applications in many scientific and engineering fields, including biomedical imaging [1], ultrasonic therapy [2,3], energy harvesting [4], nondestructive testing [5,6], and acoustic energy confinement [7], to name a few. Based on the need, numerous wave focusing methods have been devised, such as conventional curved transducer surfaces [8] like those employed in optics [9], metasurfaces [10–13], photonic crystals [4], or digital control of transducer element signals [14,15]. In practices of high-intensity focused ultrasound (HIFU), curved transducers are employed to converge acoustic waves at a focal point to thermally ablate tumors [2,16]. Although HIFU techniques are found to effectively treat cancerous tumors, it is challenging to employ the technique on tumors concealed deep in tissues [17] since the highly localized focal points have short stand-off distances from the transducers, such as in the cm scale. Digitally steered HIFU transducers offer opportunities to focus ultrasound for in vivo procedures, yet intrinsic limitations on real-time control, computational stability, and portability challenge the proliferation of digitally steered HIFU use for in vivo cancer ablation [18–20]. Thus, recent studies have proposed using shape adaptive transducers inspired by origami structures to transport HIFU devices in compacted configurations through the body to the point of care, where a deployed transducer shape is realized for treatment, prior to reversal of the shape change sequence to exit the body [17].

Origami is in fact widely considered as inspiration to devise complex three-dimensional (3D) structures that exhibit high portability by virtue of planar fabrication and folding-based shape change [21–23]. Researchers have examined origami-like folding for robotics [24,25], structural and material design [26–28], space deployable systems [29], and biomedical devices [30,31]. Origami inspiration has recently motivated explorations for acoustic wave guiding structures that may be compacted for applications with severe access limitations, such as in-the-body HIFU [17,32]. Zou and Harne [33,34] employed reconfigurable origami-based structures to realized tessellated acoustic arrays and studied the near field and far field wave radiation behaviors, revealing that curved tessellated arrays may focus acoustic waves. Srinivas and Harne [35] demonstrated that doubly curved origami-inspired arrays focus on acoustic waves using circularly symmetric array geometries. While these array structures focus on acoustic waves, the tessellations are either not flat-foldable to maximize portability or are not easily held in curved shapes indicating practical challenges. Consequently, fundamental research is needed to formulate reconfigurable origami-inspired structures that may repeatably yield curved shapes for acoustic wave focusing while providing nominal flat foldability in kinematic properties.

Motivated by the shortcomings in the state-of-the-art, this research proposes a new interface between reconfigurable mechanical structures and origami folding to yield an acoustic array with exceptional control over shape, flat foldability, and wave focusing. The proposed technique to realize focused waves is to position acoustic transducers on regular Miura-ori unit facets with folding behavior intrinsically coupled with that of a one-degree-of-freedom (1DOF) expandable structure: the Hoberman ring [36,37]. Dai et al. [38] studied the mobility of the Hoberman sphere and decomposed the structure into a four-legged platform and movable parallelogram links. Here, the Hoberman ring is utilized, which can be considered as an equatorial kinematic loop-chain in the Hoberman sphere [38]. The Hoberman ring consists of several Hoberman ring units, which are modified scissor elements in the shape of connected angulated bars. The pairs of angulated bars are connected to each other by a revolute joint, highlighted in Fig. 1(*a*) [39]. When such ring units

[1]Corresponding author.

Contributed by the Mechanisms and Robotics Committee of ASME for publication in the Journal of Mechanical Design. Manuscript received April 13, 2020; final manuscript received September 23, 2020; published online November 17, 2020. Assoc. Editor: Jian S. Dai.

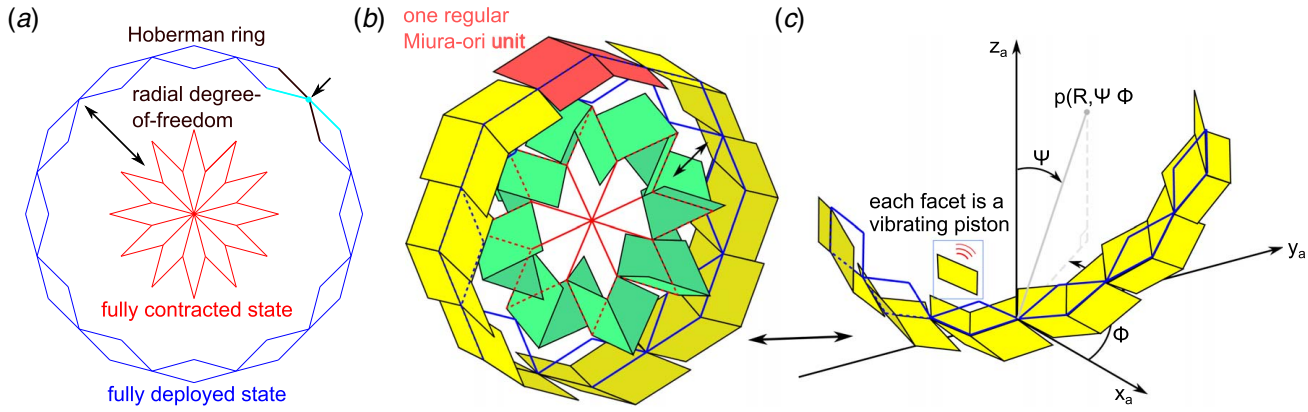

Fig. 1 (*a*) Hoberman ring in the fully contracted state and fully deployed state, (*b*) synthesized Miura-ori based, Hoberman ring mechanism with one radial degree-of-freedom, and (*c*) semi-circular acoustic array for sound wave focusing created from a segment of the full ring mechanism, where acoustic waves are generated by infinitesimal vibrations of the facets like baffled pistons

are assembled together according to requirements of kinematic compatibility, the whole Hoberman ring is a 1DOF radially deploying closed loop structure [40–42].

In this research, the angulated bars of the Hoberman ring are used as a 1DOF mechanism to control the folded configuration of wave radiating Miura-ori units (Fig. 1(*b*)). Here, the Miura-ori units are attached to the outer bar of the Hoberman ring so that folding of the Miura facet is determined by the expansion of the Hoberman ring, as shown in Fig. 1(*b*), between contracted and deployed ring configurations. Yet, a fully enclosed ring is not practical to focus acoustic waves at a distance from the array structure. As a result, the arrays considered in this research adopt the Hoberman–Miura synthesis shown in Fig. 1(*c*). An arc-shaped acoustic array of miniature vibrating Miura-ori surfaces radiates acoustic waves toward the center of the array coincident with the Hoberman ring center. In other words, by placing the Miura-ori units into the curved shape of the Hoberman ring, a wave focusing region occurs along the z-axis near to the ring center, as anticipated on the basis of geometric acoustics [8].

In this research, an analytical model is built and validated to scrutinize the wave focusing behavior of the Hoberman–Miura synthesized acoustic array. Section 2 introduces the analytical model spanning geometric and acoustic characteristics, and Sec. 3 presents experimental efforts to support salient analytical trends. Then, Sec. 4 describes theoretical investigations to uncover parametric influences of array design, driving frequency, and folding extent on wave focusing capability. Finally, the new findings of this research are summarized with concluding remarks.

2 Model Formulations

In this section, the geometric model of a controllable, reconfigurable acoustic array is developed based on an integration of the regular Miura-ori tessellation and the Hoberman ring. The geometries are first defined, after which compatibility of shape is identified. With the Miura-ori facet surfaces related to the change of Hoberman ring shape, the direct acoustic radiation from the vibrating Miura facets is found using Rayleigh's integral.

2.1 Kinematic Modeling of Hoberman Ring and Miura-Ori Integration.

The kinematic relationships among geometric parameters for Miura-ori crease patterns and Hoberman ring structures are first introduced. Figure 2(*a*) shows the geometry of a regular Miura-ori unit cell that may be repeated in x- and y-axes or altered to achieve broad curvature [43,44]. Each regular Miura-ori unit consists of four facets, such that the coordinates of the nine vertices are denoted by Eqs. (1)–(9):

$$(X_1, Y_1, Z_1) = (-S,\ L - V,\ 0) \tag{1}$$

$$(X_2, Y_2, Z_2) = (0,\ L,\ 0) \tag{2}$$

$$(X_3, Y_3, Z_3) = (S,\ L - V,\ 0) \tag{3}$$

$$(X_4, Y_4, Z_4) = (-S,\ -V,\ H) \tag{4}$$

$$(X_5, Y_5, Z_5) = (0,\ 0,\ H) \tag{5}$$

$$(X_6, Y_6, Z_6) = (S,\ -V,\ H) \tag{6}$$

$$(X_7, Y_7, Z_7) = (-S,\ -L - V,\ 0) \tag{7}$$

$$(X_8, Y_8, Z_8) = (0,\ -L,\ 0) \tag{8}$$

$$(X_9, Y_9, Z_9) = (S,\ -L - V,\ 0) \tag{9}$$

The relationships among H, S, L, and V and facet design parameter A, B, and γ and dihedral folding angle θ are given by Schenk and Guest [45], as summarized in Eqs. (10)–(13):

$$H = A \sin\theta \sin\gamma = \sqrt{A^2 - L^2} \tag{10}$$

$$S = B\frac{\cos\theta \tan\gamma}{\sqrt{1 + (\cos\theta \tan\gamma)^2}} \tag{11}$$

$$L = A\sqrt{1 - (\sin\theta \sin\gamma)^2} \tag{12}$$

$$V = B\frac{1}{\sqrt{1 + (\cos\theta \tan\gamma)^2}} \tag{13}$$

Figure 2(*b*) shows the geometry of one Hoberman ring unit [41]. As the Hoberman ring changes shape around the origin O, the nodes on the angulated bars pass through three circles with radii R_{in}, R_{mid}, and R_{out}. The relationships among the radii R_{mid} and R_{out} and the angulated bar parameters are given in Eqs. (14) and (15). As will be found in the derivation, the radius R_{in} is a design parameter of the Hoberman ring unit:

$$R_{mid} = R_{in}\cos\frac{\alpha}{2} + \sqrt{K^2 - \left[R_{in}\sin\frac{\alpha}{2}\right]^2} \tag{14}$$

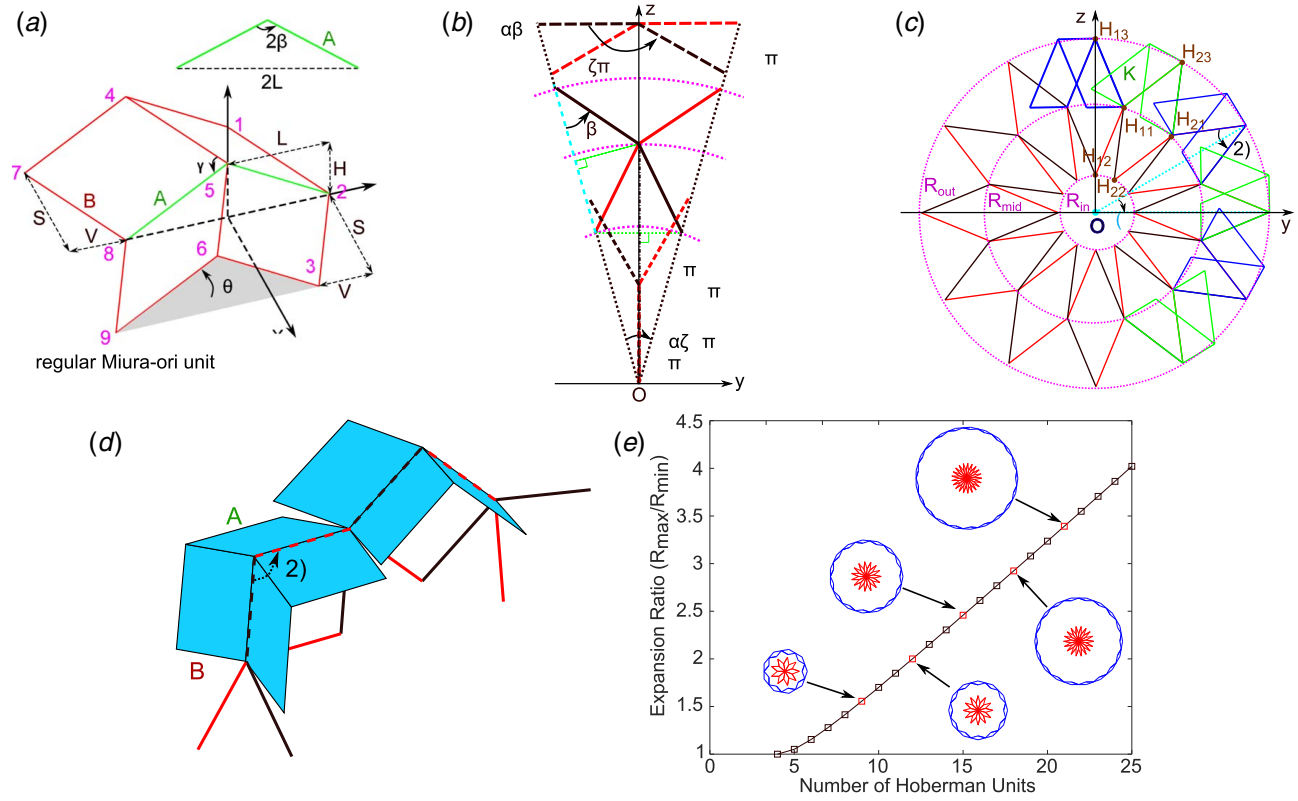

Fig. 2 (*a*) Geometry of the regular Miura-ori unit, (*b*) geometry of the Hoberman ring unit, illustration of expanding between two extremities of the Hoberman ring unit, (*c*) a 12-unit Hoberman ring with six ring units synthesized with six Miura-ori units, (*d*) schematic of synthesized Miura-ori based Hoberman ring section and related reconfiguration, and (*e*) expansion ratio of Hoberman ring as a function of number of Hoberman units in the ring

$$R_{out} = R_{in} + 2K\cos \times \left[\pi - \arcsin\left(\frac{1}{K}\sqrt{K^2 - \left[R_{in}\sin\frac{\alpha}{2}\right]^2}\right) - \frac{1}{2}(\pi - \alpha)\right] \quad (15)$$

Here, the angle α is the central angle of the Hoberman unit that remains constant during the expanding process. The angle α is determined by $\alpha = 2\pi/N$ rad, where N is the number of units in the whole ring. The K is the length of the angulated bar. Angle ζ is the obtuse angle created by the triangle defined by each identical angulated bar. The angle ζ is computed from Eq. (16):

$$2K^2(1 - \cos\zeta) = R_{in}^2 + R_{out}^2 - 2R_{in}R_{out}\cos\alpha \quad (16)$$

Angle β, shown in both Figs. 2(*a*) and 2(*b*), is defined as expansion angle, which is a parameter that connects the geometry of Hoberman ring and Miura-ori units, and it reflects both the expansion state of the Hoberman ring and folding extent of Miura-ori tessellations. The highlighted edges of the Miura-ori unit overlapped with the angulated bars of the Hoberman ring, presented in Fig. 2(*a*), show how the Miura-ori units are attached to the Hoberman ring.

To enforce geometric compatibility, the edge length A of the Miura-ori unit is the same as the angulated bar length K of the Hoberman ring, $A = K$. The Miura-ori unit and Hoberman unit are also geometrically related through expansion angle β, Eq. (17) (Fig. 2(*a*)):

$$(2L)^2 = A^2 + A^2 - 2A^2\cos 2\beta \quad (17)$$

The folding angle θ of each Miura unit is, therefore, found according to Eq. (18) by relation with the expansion angle β:

$$\sqrt{2}\sin\theta\sin\gamma = \sqrt{1 + \cos 2\beta} \quad (18)$$

The expansion angle β is related to the Hoberman ring design according to Eq. (19):

$$K\sin\left[\frac{\pi + \alpha}{2} - \beta\right] = \sqrt{K^2 - \left[R_{in}\sin\frac{\alpha}{2}\right]^2} \quad (19)$$

Based on the geometry derived above, the configuration of the Hoberman ring is uniquely defined by three independent variables: the bar length K, the Hoberman unit number N over a full circular ring, and the inner circle radius R_{in}. Based on geometric and kinematic limits, the minimum value of R_{in} is 0, while the maximum value of R_{in} is $K/[\sin(\alpha/2)] - 2K\sin(\alpha/2)$. When R_{in} reaches its maximum value, this synthesized structure is fully deployed and that facets on adjacent Miura-ori units will be coplanar. This creates a seemingly singular configuration [46,47] where adjacent Hoberman ring units have colinear angulated bars. Yet, since each Miura-ori unit is independently attached to each respective Hoberman ring unit, the collinearity of adjacent ring unit bars would not inhibit reconfiguration away from the fully deployed state. In this research, while the geometry is determined for a full Hoberman ring, only a portion of the structure is considered for acoustic purposes for sake of focusing waves radiated from the Miura-ori units that vibrate like baffled pistons.

Figure 2(*c*) shows a schematic of the synthesized mechanism while Fig. 2(*d*) provides a closer view of two units in the mechanism. The geometry of one Hoberman unit consists of nodes H_{21}, H_{12}, and H_{13}. For the convenience of calculation, the origin O is defined such that the Hoberman ring is positioned in the $y-z$ plane. As the mechanism expands and contracts, the nodal locations for H_{11}, H_{12}, and H_{13} for the first Hoberman unit are defined by Eqs. (20)–(22):

$$(x_{H_{11}}, y_{H_{11}}, z_{H_{11}}) = \left(0,\ R_{mid}\sin\frac{\alpha}{2},\ R_{mid}\cos\frac{\alpha}{2}\right) \quad (20)$$

$$(x_{H_{12}}, y_{H_{12}}, z_{H_{12}}) = (0,\ 0,\ R_{in}) \tag{21}$$

$$(x_{H_{13}}, y_{H_{13}}, z_{H_{13}}) = (0,\ 0,\ R_{out}) \tag{22}$$

Due to the rotational symmetry of the Hoberman ring, the coordinates of the remaining Hoberman ring nodes are given for the nth Hoberman unit in Eqs. (23)–(25):

$$(x_{H_{n1}}, y_{H_{n1}}, z_{H_{n1}}) = \begin{pmatrix} 0,\ R_{mid}\ \sin\dfrac{\alpha}{2}\cos[(1-n)\alpha] \\ -R_{mid}\ \cos\dfrac{\alpha}{2}\sin(1-n) + R_{mid}\ \sin\dfrac{\alpha}{2}, \\ R_{mid}\ \sin\dfrac{\alpha}{2}\sin[(1-n)\alpha] \\ +R_{mid}\ \cos\dfrac{\alpha}{2}\cos[(1-n)\alpha] + R_{mid}\ \cos\dfrac{\alpha}{2} \end{pmatrix} \tag{23}$$

$$(x_{H_{n2}}, y_{H_{n2}}, z_{H_{n2}}) = (0,\ -R_{in}\ \sin[(1-n)\alpha],\ R_{in}\ \cos[(1-n)\alpha] + R_{in}) \tag{24}$$

$$(x_{H_{n3}}, y_{H_{n3}}, z_{H_{n3}}) = (0,\ -R_{out}\ \sin[(1-n)\alpha],\ R_{out}\ \cos[(1-n)\alpha] + R_{out}) \tag{25}$$

Once the coordinates of the Hoberman ring are identified, the folding angle θ of the Miura unit is identified from Eq. (18). The nodal locations for nine vertices of the first Miura-ori unit, which is attached to the first Hoberman unit, are given by Eqs. (26)–(34):

$$(x_{11}, y_{11}, z_{11}) = \left(-S,\ R_{mid}\ \sin\frac{\alpha}{2} - V,\ R_{mid}\ \cos\frac{\alpha}{2}\right) \tag{26}$$

$$(x_{12}, y_{12}, z_{12}) = \left(0,\ R_{mid}\ \sin\frac{\alpha}{2},\ R_{mid}\ \cos\frac{\alpha}{2}\right) \tag{27}$$

$$(x_{13}, y_{13}, z_{13}) = \left(S,\ R_{mid}\ \sin\frac{\alpha}{2} - V,\ R_{mid}\ \cos\frac{\alpha}{2}\right) \tag{28}$$

$$(x_{14}, y_{14}, z_{14}) = (-S,\ -V,\ R_{out}) \tag{29}$$

$$(x_{15}, y_{15}, z_{15}) = (0,\ 0,\ R_{out}) \tag{30}$$

$$(x_{16}, y_{16}, z_{16}) = (S,\ -V,\ R_{out}) \tag{31}$$

$$(x_{17}, y_{17}, z_{17}) = (-S,\ -L - V,\ R_{out} - H) \tag{32}$$

$$(x_{18}, y_{18}, z_{18}) = (0,\ -L,\ R_{out} - H) \tag{33}$$

$$(x_{19}, y_{19}, z_{19}) = (S,\ -L - V,\ R_{out} - H) \tag{34}$$

The coordinates for the mth vertex on the nth Miura-ori unit are computed via Eq. (35), which essentially rotates the mth vertex with respect to the first Miura unit according to the positioning on the Hoberman ring

$$\begin{bmatrix} x_{nm} \\ y_{nm} \\ z_{nm} \end{bmatrix} = \begin{bmatrix} 1 & 0 & 0 \\ 0 & \cos[-(n-1)\alpha] & -\sin[-(n-1)\alpha] \\ 0 & \sin[-(n-1)\alpha] & \cos[-(n-1)\alpha] \end{bmatrix} \begin{bmatrix} x_{1m} \\ y_{1m} \\ z_{1m} \end{bmatrix} \tag{35}$$

In the mechanism shown in Fig. 2(*c*), the parameters defining the synthesized mechanism are Hoberman unit number $N = 12$, center angle $\alpha = 30$ deg, angulated bar length $K = 50$ mm, and angulated bar angle $\zeta = 150$ deg.

Although each Miura-ori unit is attached to a given Hoberman unit, the adjacent Miura-ori units are not interfaced since facet bending would be required for such a monolithic structure. Thus, the semi-circular shaped array considered here is a 1DOF deployable kinematic mechanism, with configuration defined by bar length K, Hoberman unit number N, inner radius of the Hoberman ring R_{in}, Miura side length B, and edge angle γ.

The extremity of the shape change enabled by the Hoberman–Miura synthesized mechanism is also defined. An expansion ratio is, therefore, defined as the ratio of the maximum value of the outer circle radius to the minimum value of the outer circle radius, Eq. (36):

$$\frac{R_{out\ \max}}{R_{out\ \min}} = \frac{1}{\sin\ \alpha} \tag{36}$$

In other words, the expansion ratio provided by the mechanism is determined by the Hoberman unit number N. Figure 2(*e*) presents the change of expansion ratio as a function of N. A Hoberman ring with greater number of units results in greater expansion capacity.

2.2 Acoustic Modeling and Analysis. Each Miura-ori facet is assumed to be a vibrating baffled piston, as thoroughly discussed and supported through previous research [32,17]. By virtue of this assumption, Rayleigh's integral is employed to predict the acoustic waves radiated from the Miura-ori facets that are attached to the Hoberman ring. The direct acoustic field is considered, while reflected and diffracted wave field contributions are recognized to be influential only in certain spatial and frequency regimes [48]. A spherical coordinate system is defined using a radial distance R, elevation angle ψ, and azimuth angle ϕ, as shown in Fig. 1(*c*). By Rayleigh's integral and linear superposition, the total acoustic pressure at a field point is given by Eq. (37):

$$p(R, \psi, \phi, t) = j\frac{\rho_0 \omega u_0}{2\pi} e^{j\omega t} \sum_{n=1}^{N_f} \left[\int_{A_n} \frac{e^{-jkR_n}}{R_n} dA_n \right] \tag{37}$$

The ρ_0 is the atmospheric density of the fluid medium, ω is the angular frequency, u_0 is the amplitude of the normal particle velocity of the vibrating facet, N_f is the number of facets, A_n is the area of the nth facet, $k = \omega/c_0$ is the wavenumber where c_0 is the sound speed, and R_n is the distance from the center of the nth facet to the field point. In this study, air is the fluid medium so that $\rho_0 = 1.21$ kg/m^3 and $c_0 = 343$ m/s.

A general solution to Eq. (37) may only be evaluated numerically, although the integrals become computationally challenging to converge for all field points. To surmount this limitation, this research employs the technique developed by Ocheltree and Frizzel [49] to discretize the vibrating baffled piston surfaces into a large number of discrete point sources. The distance between point sources is much less than the wavelength and much less than the facet dimensions. Consequently, upon superposition of all acoustic field contributions from each point source, an accurate representation of the direct acoustic field for the near field and far field of the array is obtained [49–52]. Thus, the discretized Rayleigh's integral to account for all point source contributions from the vibrating Miura-ori facets is Eq. (38), where A_{mn} is the mth discretized surface element on the nth facet and M is the number of discretized surfaces on a given facet:

$$p(R, \psi, \phi, t) = j\frac{\rho_0 \omega u_0}{2\pi} e^{j\omega t} \sum_{n=1}^{N_f} \sum_{m=1}^{M} \left[\frac{e^{-jkR_{mn}}}{R_{mn}} A_{mn} \right] \tag{38}$$

Once the acoustic pressure is obtained, the sound pressure level (SPL) is calculated from Eq. (39):

$$\mathrm{SPL} = 20\log_{10}\left[\frac{p_{rms}(R, \psi, \phi)}{p_{ref}}\right] \tag{39}$$

The $p_{rms}(R, \psi, \phi)$ is the root-mean-square value of $p(R, \psi, \phi)$, while $p_{ref} = 20\ \mu$Pa is the reference acoustic pressure in air.

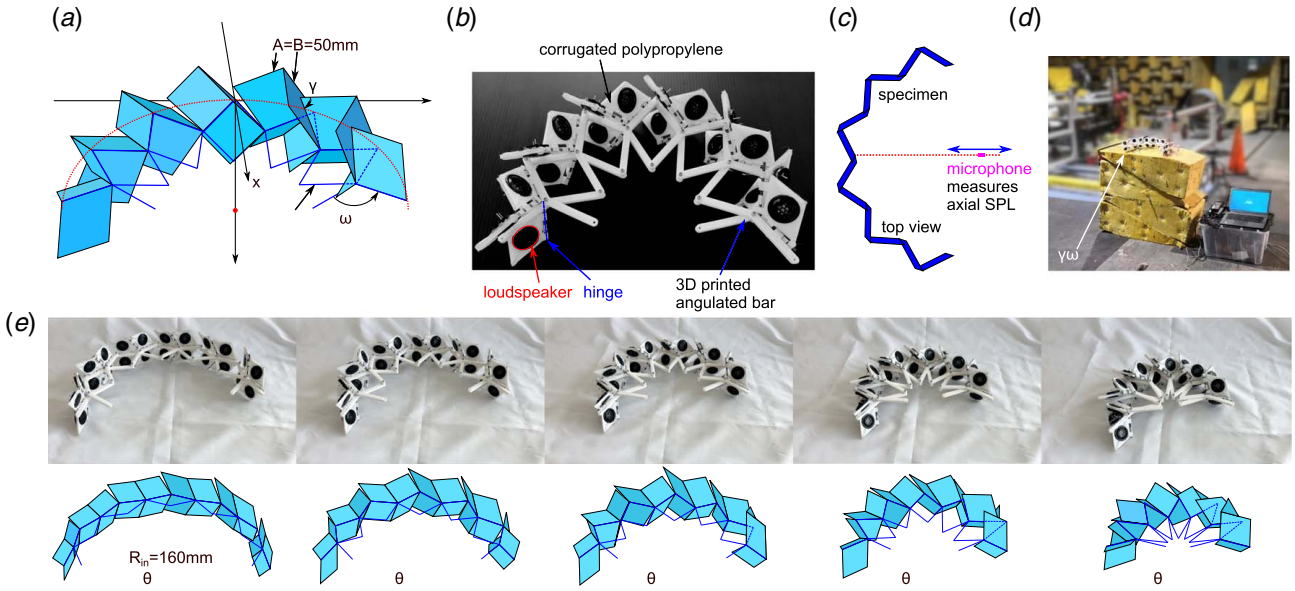

Fig. 3 (*a*) Analytical model of the semi-Hoberman ring array, with six activated Miura-ori units, (*b*) proof-of-concept specimen, (*c*) top view schematic of the experiment setup in an anechoic chamber, a microphone is employed to measure the axial SPL, (*d*) experiment setup in the hemi-anechoic chamber, and (e) specimen under five different folding states, with folding angles of 20.3 deg, 30.4 deg, 47.5 deg, 63.1 deg, and 83.7 deg

3 Experimental Validation

A proof-of-concept specimen is designed and fabricated to undertake experimental validation efforts for the analytical model. The comparison of analytical and experimental results is reported in this section.

3.1 Experimental Proof-of-Concept Array of Hoberman–Miura Wave Radiating Units. Figure 3(*a*) provides a schematic representation of the array structure represented by the proof-of-concept specimen shown in Fig. 3(*b*). The mechanism employs six Miura-ori units each attached to a Hoberman ring unit that are, respectively, connected in series. The facet dimensions of the Miura-ori units are $B = 50$ mm and $\gamma = 70$ deg. The Miura-ori facets are composed of corrugated polypropylene with square cross section flutes of square edge length 5 mm. The thickness of the polypropylene sheet in the corrugations is 0.3 mm. The polypropylene sheets shaped by the laser cutter (Epilog Laser Mini 24) and then assembled. Each Miura-ori unit cell is made of four facets, and each facet is made of four laser cut sub-facets that are adhered together in the facet shape with a miniature 2.5 cm diameter loudspeaker (Parts Express) at the center. The dimensions of the Hoberman ring are $N = 12$, bar length $K = 50$ mm, $\zeta = 150$ deg, although only six of the 12 units are used in the proof-of-concept specimen. The angulated bars of the Hoberman ring are printed by a 3D printer (FlashForge Creator Pro) using acrylonitrile butadiene styrene (ABS) and are fastened together. The Miura-ori facets are attached to the Hoberman units by inserting threaded rods into the fluted, square-shaped edges of the Miura-ori facets and the flutes on the angulated Hoberman bars. The threaded rods function as hinges to enforce revolute joint behavior required for the Miura folding process compatible with the expansion process of the Hoberman ring. The miniature loudspeakers are driven by the external amplifier with the same signal. Figure 3(*e*) verifies the shape change of the analytical representation of the array alongside the experimental photos of the deployed and contracted configurations of the Hoberman–Miura proof-of-concept specimen.

3.2 Experimental Methods. Experiments are conducted inside a hemi-anechoic chamber, with interior dimensions of 7.78 m, 10.9 m, and 4.66 m, as shown in Fig. 3(*d*). The specimen is affixed to fiberglass wedge surfaces to serve as a baffled backing. The folded angle of the array is measured directly. A microphone (PCB Piezotronics, Depew, NY, 130E20) is used to measure the axial acoustic pressure of the array, as shown in Fig. 3(*c*). A displacement sensor (WDS-1500-P60-SR-U, SN 51712) is used to directly measure the axial location of the microphone. The microphone measures the axial acoustic pressure in the azimuthal angle $\phi = 0$ deg. A single frequency signal is sent to an audio amplifier that drives the array loudspeakers. Measurements from the microphone are post-processed by MATLAB to determine the acoustic pressure amplitude and sound pressure level that is recorded along the axial distance.

3.3 Experimental and Analytical Result Comparisons. Figure 4 presents a comparison between experimental and analytical results. The normal velocity amplitude used in the analytical model is determined empirically to be 0.6 mm/s. In Fig. 4(*a*), the folding angle of the array is $\theta = 71.55$ deg and the driving frequency is 4 kHz. For this condition, the peak of SPL is 92 dB around $R = 0.080$ m. As the frequency is increased to 5 kHz and 6 kHz, the axial acoustic SPL peak reduces to 91 dB and 88 dB, respectively, at axial distances near $R = 0.085$ m and $R = 0.09$ m, locations more distance from the origin than the focal point at 4 kHz. Figure 4(*c*) shows the corresponding experimental results. The results suggest that when driven by 4 kHz, the axial SPL peak reaches around 91 dB at $R = 0.08$ m. When the driving frequencies are 5 kHz and 6 kHz, the axial SPL peaks are 92 dB and 90 dB, respectively, both peaks occurring at $R = 0.11$ m. Compared with Fig. 4(*a*), the focusing trends qualitatively agree, although inability to exactly realize the ideal model geometry through the proof-of-concept array and precise environmental conditions lead to discrepancies with exact SPL and distance values. In other words, the miniature loudspeakers do not fully activate the Miura-ori facet surfaces of the array, which contributes to imprecise realization of the modeled ideal Hoberman–Miura synthesized array. In addition, mounting of the array in the hemi-anechoic environment is unable to perfectly simulate anechoic conditions, thus leading to minor room reflections that degrade measurements, especially at low SPL values such as for axial distances greater than 0.35 m. Yet, there is

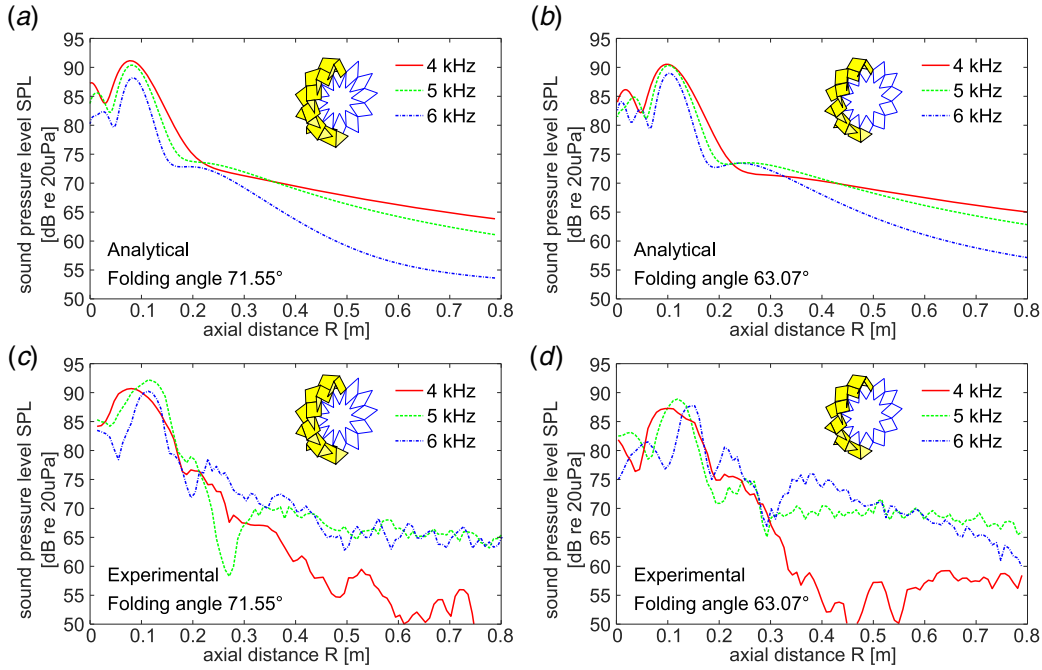

Fig. 4 Comparison between experimental and analytical results of SPL as a function of axial distance: (*a* and *b*) analytical results of the axial SPL as a function of axial distance, with different folding angles and (*c* and *d*) experimental SPL

strong overall qualitative agreement of predicted behavior as observed experimentally, especially nearer to the focal point.

Figure 4(*b*) shows the axial SPL as a function of axial distance for a smaller value of folding angle 63.07 deg. The three SPL peaks at 4, 5, and 6 kHz occur near $R = 0.1$ m, with the peak SPL value of about 91, 90, and 89 dB, respectively. The focusing characteristics for folding angle 63.07 deg in Fig. 4(*b*) are similar to those for folding angle 71.55 deg in Fig. 4(*a*). Experimental results for the folding angle 63.07 deg are likewise shown in Fig. 4(*d*). Here, the trends of focal point locations increasing with increase of frequency observed analytically are also seen experimentally. These results confirm the efficacy of the analytical model to predict the salient near field behaviors of a proof-of-concept Hoberman–Miura synthesized acoustic array, despite inability to fabricate an ideal experimental specimen. With such foundation in place, it remains to investigate design techniques by which the synthesized mechanism is constructed maintaining kinematic compatibility while acoustic wave focusing is maintained.

4 Exploring Wave Focusing Methods Using a Hoberman–Miura Synthesized Array

In this section, the analytical model is employed to gain insight on combined acoustic and mechanical geometries that enable wave focusing behaviors via the Hoberman–Miura synthesized array. Sections 4.1–4.4 investigate design and operational parameters relevant to wave focusing provided by the array.

4.1 Mechanism Expansion and Folding Angle Effects on Acoustic Wave Focusing. The influence on array expansion or folding on the focal point SPL is investigated. Here, an array is considered using six Hoberman–Miura units assembled as shown in the insets of Fig. 5. The bar length is $K = 50$ mm, obtuse angle $\zeta = 150$ deg, the Miura facet edge length is $B = 50$ mm, and the edge angle is $\gamma = 70$ deg. Figures 5(*a*)–5(*c*) present the results of axial SPL for driving frequencies 4 kHz, 5 kHz, and 6 kHz, respectively, with five different folding angles in each sub-figure. The five folding angles are determined by the inner radii of the Hoberman ring, which are 40 mm, 50 mm, 60 mm, 70 mm, and 80 mm, respectively. In each sub-figure, the line styles indicate the folding extents of the array, while the inset images illustrate the array when folded to $\theta = 71.5$ deg so that the inner radius of the Hoberman ring is 40 mm.

In Fig. 5(*a*) for a driving frequency value of 4 kHz, as the Hoberman ring expands, which occurs for smaller folding angle, the SPL focal point location increases from 0.08 m to 0.12 m. In Figs. 5(*b*) and 5(*c*), similar trends are observed at 5 kHz and 6 kHz, respectively. On the other hand, the respective changes of focal point SPL value with change in array configuration differ based on the wave interference corresponding to the driving frequency. For instance, the focal points at 4 kHz in Fig. 5(*a*) reduce from 91 dB to 90 dB as the folding angle decreases from 71.5 deg to 55.2 deg, while at 6 kHz in Fig. 5(*c*), the peak SPL values increase from 87 dB to 89 dB. By contrast, at 5 kHz in Fig. 5(*b*), there is no quantitative change in focal point SPL as the Hoberman–Miura mechanism is reconfigured over the range studied. These distinctions indicate that near field interference in this frequency range affects stability of acoustic energy delivery to the focal point.

In these examples, 5 kHz is the exemplary frequency for which small controlled changes of the array shape by the mechanism expansion and contraction do not appreciably influence the sound pressure level received at the focal point. Despite the frequency-dependent behavior, for this Hoberman–Miura synthesized acoustic array, the focusing behavior leads to around 6 dB increase in SPL (around three times increase in pressure amplitude) at the focal point compared with the SPL close to the surface and center of the array.

4.2 Activation of Array Facets Across a Frequency Bandwidth. In this section, the sensitivity of peak axial SPL resulting from changes to the driving frequency and number of activated sound radiating facets is examined. The synthesized acoustic array studied here employs 12 Hoberman ring units, bar length $K =$ 50 mm, $B = 50$ mm, and edge angle $\gamma = 70$ deg. In Fig. 6(*a*), the folding angle is $\theta = 33.86$ deg. The insets show that each line style represents an array containing either 4, 6, or 8 activated Miura-ori units attached to the Hoberman ring. For greater numbers of activated Miura-ori units, the peak SPL values increase, which is consistent in Figs. 6(*b*) and 6(*c*) for folding angles $\theta =$

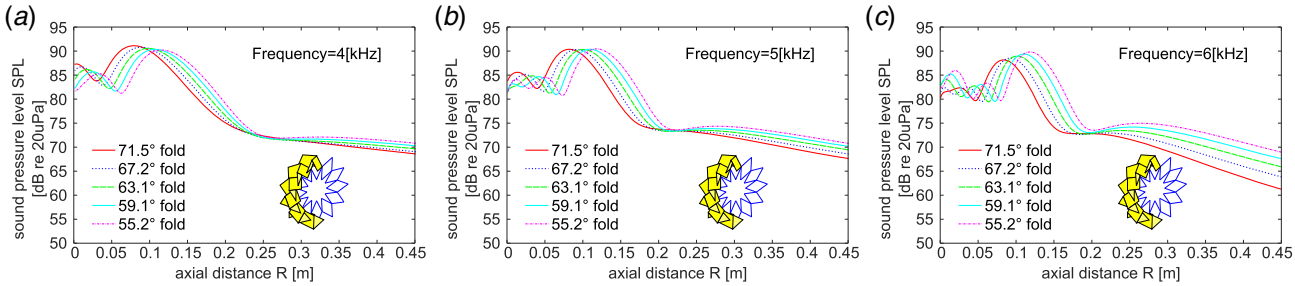

Fig. 5 Folding influence on acoustic wave focusing. Driving frequencies for the array are (*a*) 4 kHz, (*b*) 5 kHz, and (*c*) 6 kHz. In each sub-figure, the folding angles θ shown by line styles are 71.5 deg, 67.2 deg, 63.1 deg, 59.1 deg, and 55.2 deg.

44.68 deg and 58.29 deg, respectively. This confirms a general intuition that for sound focusing wave radiators, the greater the vibrating surfaces are, the greater sound pressure amplitudes will be the focal point. In Fig. 6(*a*), regardless of folding angle, the driving frequency increase results in the increase of focal point SPL. In Figs. 6(*b*) and 6(*c*), frequencies are observed where the peak axial SPL values reach maxima. Because the radiating surfaces of the Miura-ori units do not direct point to the focal point, destructive interference phenomena occur in close relation with the wavelength. This causes frequency-dependent focal point SPL, especially when the array is highly folded as shown in Fig. 6(*c*). In absence of this unique characteristic of the Hoberman–Miura synthesized acoustic array, the pressure amplitude at the focal point of a nominally ideal spherical or arc-shaped sound radiator uniformly increases with increase in frequency [8].

4.3 Influence of Hoberman Unit Numbers on the Wave Focusing Capability. As shown in Fig. 2(*e*), greater number N of Hoberman ring units results in greater expansion ratio between deployed and contracted states, which has a variety of practical benefits. Consequently, it is needed to illuminate how the number of ring units N in the synthesized acoustic array tailors wave focusing capability. Here, throughout Fig. 7, each array considered employs eight activated Miura-ori units while the number of ring units varies, thus governing the overall array shape as shown through inset schematics in Fig. 7. In all cases in Fig. 7, the folding angle is 60 deg and the driving frequency is 4 kHz. The results in Fig. 7 are shown as a function of normalized axial distance R/R_{in} since the absolute focal point locations change for change in ring number N.

It is observed in Fig. 7 that as a greater number of Hoberman ring units are employed, the focal point SPL value decreases. This result is intuitive because the radius of curvature of the array decreases with fewer ring units N, and a greater proportion of an arc activated around a focal point will nominally increase sound pressure amplitude at the focus [50]. Figure 7(*a*) also indicates that the peak SPL of each Hoberman ring number value occurs at a normalized radial distance around 1, demonstrating that the focal point of the synthesized arrays consistently occurs around the center of the semi-Hoberman ring mechanism.

Both these trends of focal point position and focal point SPL are confirmed for driving frequencies 5 kHz and 6 kHz, as shown in Figs. 7(*b*) and 7(*c*), respectively. The results present intuitive findings in multiple respects. First, the focal point is nominally at the geometric acoustic center [8], which is the center of the semi-Hoberman ring mechanism in these studies. Second, the reduction of SPL at the focal point for increasing number N of Hoberman ring units is intuitive because the Miura-ori units are more distant to the focusing center for larger values of N. Thus, while greater values of N for the Hoberman ring assembly lead to increased shape change, a similarly greater number of Miura-ori units must be used to retain high focal SPL for the acoustic array implementation.

4.4 Discussion, Multi-Dimensional Concept Extension, and Practical Assessments. In Secs. 4.1–4.3, the deployability and acoustic focusing capability of the Hoberman–Miura synthesized array is examined from the standpoints of design and implementation. Here, the primary findings are summarized and considered in an extension of the concept to multidimensional arrays.

By leveraging the straightforward 1DOF reconfiguration of the Hoberman mechanism, this research identifies a potential means to control the shape change of wave focusing origami-inspired acoustic arrays. By enforcing kinematic compatibility between Miura-ori facet and Hoberman ring unit cells, the synthesized mechanism created here provides inspiration for other researchers seeking programmed shape change functionality for origami tessellations. For a partial ring of the Hoberman–Miura synthesized acoustic array, the unique tessellated sound radiating facets do not propagate and focus acoustic waves in a way precisely

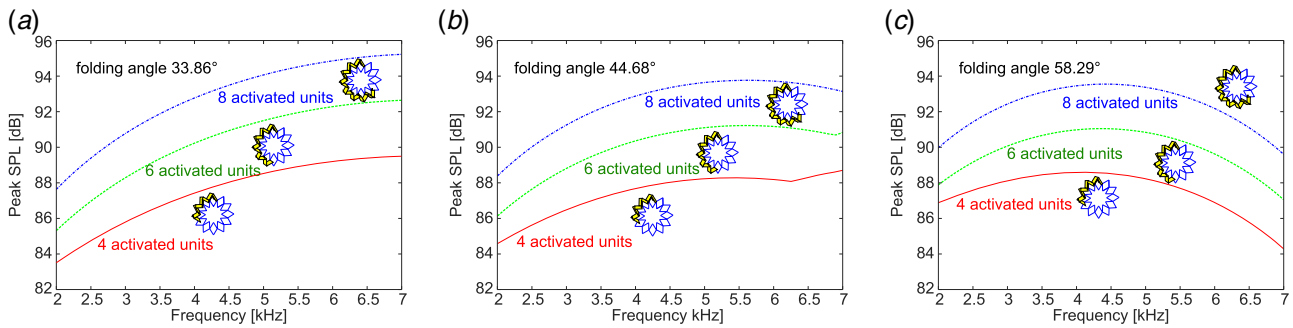

Fig. 6 Focal point SPL as a function of driving frequency of the synthesized array. Array with (*a*) folding angle of 33.86 deg, (*b*) folding angle of 44.68 deg, and (c) folding angle of 58.29 deg. Line styles indicate different numbers of activated Miura-ori units attached to the 12-unit Hoberman ring.

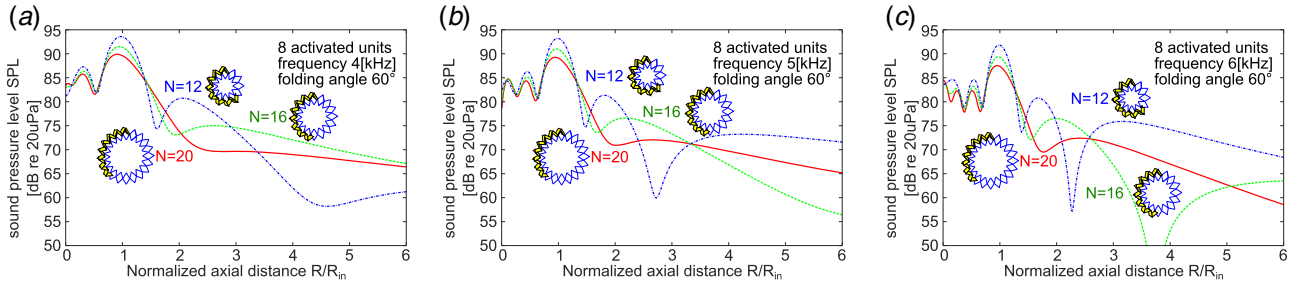

Fig. 7 Axial SPL as a function of normalized axial distance. Arrays with eight activated Miura-ori units, each with the folding angle of 60 deg are tested at driving frequency of (*a*) 4 kHz, (*b*) 5 kHz, and (*c*) 6 kHz. Line styles and insets indicate Hoberman rings with three different Hoberman ring numbers that the eight Miura-ori units are attached to.

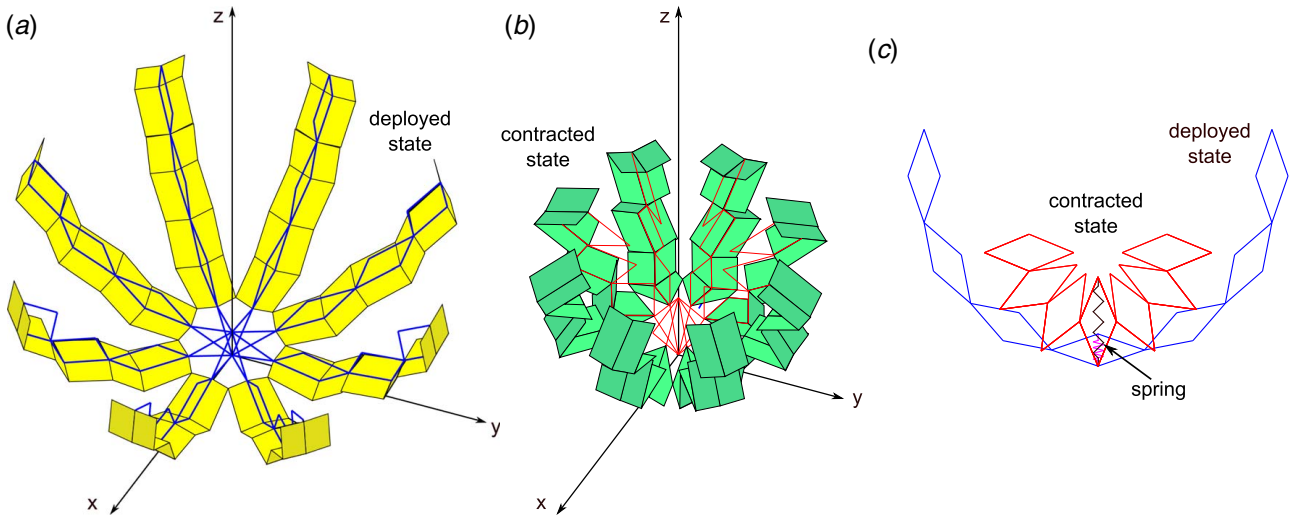

Fig. 8 Overview of a 3D Hoberman ring mechanism: (*a* and *b*) illustration of the contracted and deployed states of the 3D acoustic array and (*c*) cross-section of the mechanism employed to control the expansion of the array

analogous to geometrical acoustics. Due to inwardly directed facets, sound focusing by the proposed array exhibits frequency dependence that is atypical for nominal ring-shaped sound radiators, although reports indicate that sound focusing gains are as substantial as for the ideal acoustic geometries [50,35]. Through the example synthesized array studied in this report, greater varieties of origami-mechanism integrations may be uncovered and explored for distinctive application needs.

Here, it is found that the acoustic array creates a focal point at the center of the Hoberman ring mechanism and that the position of the focal point is manipulated by expansion and contraction of the ring. Figure 8 gives an illustration of how this concept may be extended to the design of the Hoberman sphere [38], using a part spherical region as the functional surface to be used for sake of an acoustic array platform. Figure 8(*a*) shows representative contracted and deployed states of a Hoberman sphere-based extension of the concept studied here, featuring four rings of the Hoberman–Miura synthesized mechanism radially extending from a shared nodal location on a Hoberman sphere. According to Dai et al. [38], the shared node at the origin can be designed as a stable, eight-legged platform, while the Hoberman rings are guided in the deployed and contraction process by the linkages. As shown in the cross-sectional view in Fig. 8(*b*), each ring contains seven Hoberman–Miura units. Since the mechanism has a shared central unit, one means of practically changing the shape of the array is to centrally locate a linear actuator or spring as shown in Fig. 8(*b*). While there are potentially numerous embodiments of such actuation, this research exemplifies that versatile reconfigurable structures like the Hoberman mechanism may be exploited for sake of changing the shape of origami-inspired devices, here studied in the context of acoustic arrays.

5 Conclusion

This research explores an interface between reconfigurable structures and origami devices to propose a concept for reconfigurable tessellated acoustic arrays with straightforward shape change for sound focusing. By establishing kinematic and geometric compatibility between a Hoberman ring unit and Miura-ori unit for sound radiation, a reconfigurable acoustic array is assembled and investigated. Following experimental validation of salient model trends, the influences of wave focusing governed by array geometry are investigated. The results reveal similarities between geometric acoustics and the proposed tessellated array approach as well as uncover principles that balance synthesized mechanism simplicity with the effectiveness of wave focusing. The significance of this research is an exemplary integration of kinematic mechanisms with origami adaptive systems with first application to wave focusing structures where controllable curvatures are central to focusing properties. This research motivates other mechanism-tessellation integrations where low degree-of-freedom shape change of origami devices is desired.

Acknowledgment

This project is supported by the National Science Foundation Faculty Early Career Development Award (No. 1749699).

Conflict of Interest

There are no conflicts of interest.

Data Availability Statement

The datasets generated and supporting the findings of this article are obtainable from the corresponding author upon reasonable request. The authors attest that all data for this study are included in the paper.

References

[1] Tanter, M., and Fink, M., 2014, "Ultrafast Imaging in Biomedical Ultrasound," IEEE Trans. Ultrason. Ferroelectr. Freq. Control, **61**(1), pp. 102–119.

[2] van den Bijgaart, R. J., Eikelenboom, D. C., Hoogenboom, M., Fütterer, J. J., den Brok, M. H., and Adema, G. J., 2017, "Thermal and Mechanical High-Intensity Focused Ultrasound: Perspectives on Tumor Ablation, Immune Effects and Combination Strategies," Cancer Immunol. Immunother., **66**(2), pp. 247–258.

[3] Maloney, E., and Hwang, J. H., 2015, "Emerging HIFU Applications in Cancer Therapy," Int. J. Hyperthermia, **31**(3), pp. 302–309.

[4] Tol, S., Degertekin, F. L., and Erturk, A., 2017, "Phononic Crystal Luneburg Lens for Omnidirectional Elastic Wave Focusing and Energy Harvesting," Appl. Phys. Lett., **111**(1), p. 013503.

[5] Komura, I., Hirasawa, T., Nagai, S., Takabayashi, J., and Naruse, K., 2001, "Crack Detection and Sizing Technique by Ultrasonic and Electromagnetic Methods," Nucl. Eng. Des., **206**(2–3), pp. 351–362.

[6] Kim, H., Jhang, K., Shin, M., and Kim, J., 2006, "A Noncontact NDE Method Using a Laser Generated Focused-Lamb Wave With Enhanced Defect-Detection Ability and Spatial Resolution," NDT&E Int., **39**(4), pp. 312–319.

[7] Qi, S., Li, B., and Assouar, B., 2017, "Acoustic Focusing and Energy Confinement Based on Multilateral Metasurfaces," Phys. Rev. Appl., **7**(5), p. 054006.

[8] O'Neil, H. T., 1949, "Theory of Focusing Radiators," J. Acoust. Soc. Am., **21**(5), pp. 516–526.

[9] Born, M., and Wolf, E., 1999, *Principles of Optics: Electromagnetic Theory of Propagation, Interference and Diffraction of Light*, Cambridge University Press, Cambridge.

[10] Zhu, H., Walsh, T. F., and Semperlotti, F., 2018, "Total-Internal-Reflection Elastic Metasurfaces: Design and Application to Structural Vibration Isolation," Appl. Phys. Lett., **113**(22), p. 221903.

[11] Jiang, X., Shi, C., Wang, Y., Smalley, J., Cheng, J., and Zhang, X., 2020, "Nonresonant Metasurface for Fast Decoding in Acoustic Communications," Phys. Rev. Appl., **13**(1), p. 014014.

[12] Zhao, S. D., Chen, A. L., Wang, Y. S., and Zhang, C., 2018, "Continuously Tunable Acoustic Metasurface for Transmitted Wavefromt Modulation," Phys. Rev. Appl., **10**(5), p. 054066.

[13] Dubois, M., Shi, C., Wang, Y., and Zhang, X., 2017, "A Thin and Conformal Metasurface for Illusion Acoustics of Rapidly Changing Profiles," Appl. Phys. Lett., **110**(15), p. 151902.

[14] Van Veen, B. D., and Buckley, K. M., 1988, "Beamforming: A Versatile Approach to Spatial Filtering," IEEE ASSP Mag., **5**(2), pp. 4–24.

[15] Marzo, A., Seah, S. A., Drinkwater, B. W., Sahoo, D. R., Long, B., and Subramanian, S., 2015, "Holographic Acoustic Elements for Manipulation of Levitated Objects," Nat. Commun., **6**(1), p. 8661.

[16] Canney, M. S., Bailey, M. R., Crum, L. A., Khokhlova, V. A., and Sapozhnikov, O. A., 2008, "Acoustic Characterization of High Intensity Focused Ultrasound Fields: A Combined Measurement and Modeling Approach," J. Acoust. Soc. Am., **124**(4), pp. 2406–2420.

[17] Zou, C., and Harne, R. L., 2020, "Deployable Tessellated Transducer Array for Ultrasound Focusing and Bio-Heat Generation in a Multilayer Environment," Ultrasonics, **104**, p. 106108.

[18] Zou, C., and Harne, R. L., 2017, "Adaptive Acoustic Energy Delivery to Near and Far Fields Using Foldable, Tessellated Star Transducers," Smart Mater. Struct., **26**(5), p. 055021.

[19] Johnson, D. H., and Dudgeon, D. E., 1993, *Array Signal Processing: Concepts and Techniques*, Prentice Hall, Englewood Cliffs.

[20] Jensen, J. A., Holten-Lund, H., Nilsson, R., Hansen, M., Larsen, U., Domsten, R., Tomov, B., Stuart, M., Nikolov, S., Pihl, M., Du, Y., and Rasmussen, J., 2013, "SARUS: A Synthetic Aperture Real-Time Ultrasound System," IEEE Trans. Ultrason. Ferroelectr. Freq. Control, **60**(9), pp. 1838–1852.

[21] Gillman, A., Fuchi, K., and Buskohl, P. R., 2018, "Truss-Based Nonlinear Mechanical Analysis for Origami Structures Exhibiting Bifurcation and Limit Point Instabilities," Int. J. Solids Struct., **147**, pp. 80–93.

[22] Li, S., Fang, H., Sadeghi, S., Bhovad, P., and Wang, K. W., 2019, "Architected Origami Materials: How Folding Creates Sophisticated Mechanical Properties," Adv. Mater., **31**(5), p. 1805282.

[23] Chen, Y., Sareh, P., Yan, J., Fallah, A. S., and Feng, J., 2019, "An Integrated Geometric-Graph-Theoretic Approach to Representing Origami Structures and Their Corresponding Truss Frameworks," ASME J. Mech. Des., **141**(9), p. 091402.

[24] Miyashita, S., Guitron, S., Li, S., and Rus, D., 2017, "Robotic Metamorphosis by Origami Exoskeletons," Sci. Rob., **2**(10), p. eaao4369.

[25] Pooya, S., Chermprayong, P., Emmanuelli, M., Nadeem, H., and Kovac, M., 2018, "Rotorigami: A Rotary Origami Protective System for Robotic Rotorcraft," Sci. Rob., **3**(22), pp. eaah5228.

[26] Peraza-Hernandez, E. A., Hartl, D. J., Malak, R. J., and Lagoudas, D. C., 2014, "Origami-Inspired Active Structures: A Synthesis and Review," Smart Mater. Struct., **23**(9), p. 094001.

[27] Zadpoor, A. A., 2016, "Mechanical Meta-Materials," Mater. Horiz., **3**(5), pp. 371–381.

[28] Wei, G., and Dai, J., 2014, "Origami-Inspired Integrated Planar-Spherical Overconstrained Mechanisms," ASME J. Mech. Des., **136**(5), p. 051003.

[29] Zirbel, S. A., Lang, R. J., Thomson, M. W., Sigel, D. A., Walkemeyer, P. E., Trease, B. P., Magleby, S. P., and Howell, L. L., 2013, "Accommodating Thickness in Origami-Based Deployable Arrays," ASME J. Mech. Des., **135**(11), p. 111005.

[30] Rothemund, P. W. K., 2006, "Folding DNA to Create Nanoscale Shapes and Patterns," Nature, **440**(7082), pp. 297–302.

[31] Dutta, P. K., Zhang, Y., Blanchard, A. T., Ge, C., Rushdi, M., Weiss, K., Zhu, C., Ke, Y., and Salaita, K., 2018, "Programmable Multivalent DNA-Origami Tension Probes for Reporting Cellular Traction Forces," Nano Lett., **18**(8), pp. 4803–4811.

[32] Harne, R. L., and Lynd, D. T., 2016, "Origami Acoustics: Using Principles of Folding Structural Acoustics for Simple and Large Focusing of Sound Energy," Smart Mater. Struct., **25**(8), p. 085031.

[33] Zou, C., and Harne, R. L., 2018, "Piecewise Assembled Acoustic Arrays Based on Reconfigurable Tessellated Structures," J. Acoust. Soc. Am., **144**(4), pp. 2324–2333.

[34] Zou, C., and Harne, R. L., 2017, "Adaptive Acoustic Energy Delivery to Near and Far Fields Using Foldable, Tessellated Star Transduceres," Smart Mater. Struct., **26**(5), p. 055021.

[35] Srinivas, V., and Harne, R. L., 2020, "Acoustic Wave Focusing by Doubly Curved Origami-Inspired Arrays," J. Int. Mater. Syst. Struct, **31**(8), pp. 1041–1052.

[36] Hoberman, C. Reversibly Expandable Doubly-Curved Truss Structure. U.S. Patent No. 4942700. 1990 July 24.

[37] Wei, G., Ding, X., and Dai, J. S., 2010, "Mobility and Geometric Analysis of the Hoberman Switch-Pitch Ball and Its Variant," ASME J. Mech. Rob., **2**(3), p. 031010.

[38] Dai, J., Li, D., Zhang, Q., and Jin, G., 2004, "Mobility Analysis of a Complex Structured Ball Based on Mechanism Decomposition and Equivalent Screw System Analysis," Mech. Mech. Theory, **39**(4) pp. 445–458.

[39] Maden, F., Korkmaz, K., and Akgün, Y., 2011, "A Review of Planar Scissor Structural Mechanisms: Geometric Principles and Design Methods," Architect. Sci. Rev., **54**(3), pp. 246–257.

[40] Yar, M., Korkmaz, K., Kiper, G., Maden, F., Akgün, Y., and Aktaş, E., 2017, "A Novel Planar Scissor Structure Transforming Between Concave and Convex Configuration," Int. J. Comput. Methods Exp. Meas., **5**(4), pp. 442–450.

[41] You, Z., and Pellegrino, S., 1997, "Foldable Bar Structures," Int. J. Solids Struct., **34**(15), pp. 1825–1847.

[42] Patel, J., and Ananthasuresh, G. K., 2007, "A Kinematic Theory for Radially Foldable Planar Linkages," Int. J. Solids Struct., **44**(18–19), pp. 6279–6298.

[43] Gattas, J. M., Wu, W., and You, Z., 2013, "Miura-Based Rigid Origami: Parameterizations of First-Level Derivative and Piecewise Geometries," ASME J. Mech. Des., **135**(11), p. 111011.

[44] Dudte, L. H., Vouga, E., Tachi, T., and Mahadevan, L., 2016, "Programming Curvature Using Origami Tessellations," Nat. Mater., **15**(5), pp. 583–588.

[45] Schenk, M., and Guest, S. D., 2013, "Geometry of Miura-Folded Metamaterials," Proc. Natl. Acad. Sci. USA, **110**(9), pp. 3276–3281.

[46] Wei, G., Chen, Y., and Dai, J. S., 2014, "Synthesis, Mobility, and Multifurcation of Deployable Polyhedral Mechanisms With Radially Reciprocating Motion," ASME J. Mech. Des., **136**(9), p. 091003.

[47] Chen, Y., Feng, J., and Sun, Q., 2018, "Lower-Order Symmetric Mechanism Modes and Bifurcation Behavior of Deployable Bar Structures With Cyclic Symmetry," Int. J. Solids Struct., **139-140**, pp. 1–14.

[48] Zou, C., and Harne, R. L., 2019, "Tailoring Reflected and Diffracted Wave Fields From Tessellated Acoustic Arrays by Origami Folding," Wave Motion, **89**, pp. 193–206.

[49] Ocheltree, K. B., and Frizzel, L. A., 1989, "Sound Field Calculationg for Rectangular Sources," IEEE Trans. Ultrason. Ferroelectr. Freq. Control, **36**(2), pp. 242–248.

[50] Zou, C., Lynd, D. T., and Harne, R. L., 2018, "Acoustic Wave Guiding by Reconfigurable Tessellated Arrays," Phys. Rev. Appl., **9**(1), p. 014009.

[51] Ebbini, E. S., and Cain, C. A., 1991, "A Spherical-Section Ultrasound Phased Array Applicator for Deep Localized Hyperthermia," IEEE Trans. Biomed. Eng., **38**(7), pp. 634–643.

[52] Jensen, J. A., and Svendsen, N. B., 1992, "Calculation of Pressure Fields From Arbitrarily Shaped, Apodized, and Excited Ultrasound Transducers," IEEE Trans. Ultrason. Ferroelectr. Freq. Control, **39**(2), pp. 262–267.